

Article

MnO_x Supported on Hierarchical SAPO-34 for the Low-Temperature Selective Catalytic Reduction of NO with NH₃: Catalytic Activity and SO₂ Resistance

Lusha Zhou¹, Jinkun Guan¹, Chenglong Yu² and Bichun Huang^{1,*} 

¹ Guangzhou Higher Education Mega Centre, School of Environment and Energy, South China University of Technology, Guangzhou 510006, China; es201821035437lusa@mail.scut.edu.cn (L.Z.); esguanjk@mail.scut.edu.cn (J.G.)

² School of Land Resources and Environment, Jiangxi Agricultural University, Nanchang 330045, China; hjclyu@jxau.edu.cn

* Correspondence: cebhuang@scut.edu.cn; Tel.: +86-020-33501289

Abstract: The ethanol dispersion method was employed to synthesize a series of MnO_x/SAPO-34 catalysts using SAPO-34 with the hierarchical pore structure as the zeolite carrier, which were prepared by facile acid treatment with citric acid. Physicochemical properties of catalysts were characterized by XRD, XPS, BET, TEM, NH₃-TPD, SEM, FT-IR, Py-IR, H₂-TRP and TG/DTG. NH₃-SCR performances of the hierarchical MnO_x/SAPO-34 catalysts were evaluated at low temperatures. Results show that citric acid etching solution at a concentration of 0.1 mol/L yielded a hierarchical MnO_x/SAPO-34-0.1 catalyst with *ca.*15 wt.% Mn loading, exhibiting optimal catalytic activity and SO₂ tolerance at low temperatures. Almost 100% NO conversion and over 90% N₂ selectivity at 120 °C under a gas hourly space velocity (GHSV) of 40,000 h⁻¹ could be obtained over this sample. Furthermore, the NO conversion was still higher than 65% when 100 ppm SO₂ was introduced to the reaction gas for 4 h. These could be primarily attributed to the large specific surface area, high surface acidity concentration and abundant chemisorbed oxygen species provided by the hierarchical pore structure, which could also increase the mass transfer of the reaction gas. This finding suggests that the NH₃-SCR activity and SO₂ poisoning tolerance of hierarchical MnO_x/SAPO-34 catalysts at low temperatures can be improved by controlling the morphology of the catalysts, which might supply a rational strategy for the design and synthesis of Mn-based SCR catalysts.

Keywords: hierarchical SAPO-34; manganese oxides; low-temperature NH₃-SCR; molecular sieves; SO₂ resistance



Citation: Zhou, L.; Guan, J.; Yu, C.; Huang, B. MnO_x Supported on Hierarchical SAPO-34 for the Low-Temperature Selective Catalytic Reduction of NO with NH₃: Catalytic Activity and SO₂ Resistance. *Catalysts* **2021**, *11*, 314. <https://doi.org/10.3390/catal11030314>

Academic Editors:

Fabio Alessandro Deorsola and Lidia Castoldi

Received: 22 January 2021

Accepted: 23 February 2021

Published: 27 February 2021

Publisher's Note: MDPI stays neutral with regard to jurisdictional claims in published maps and institutional affiliations.



Copyright: © 2021 by the authors. Licensee MDPI, Basel, Switzerland. This article is an open access article distributed under the terms and conditions of the Creative Commons Attribution (CC BY) license (<https://creativecommons.org/licenses/by/4.0/>).

1. Introduction

Nitrogen oxides (NO_x), which are released from stationary and automobile exhausts, are major atmospheric pollutants that result in many environmental issues, such as haze, acid rain and photochemical smog [1]. To date, the best developed and most efficient flue gas cleaning technology for NO_x abatement from stationary sources is the selective catalytic reduction (SCR) of NO_x with ammonia [2–4]. Owing to their high efficiency in eliminating NO_x, V₂O₅-WO₃/TiO₂ catalysts have been used commercially as an NH₃-SCR catalyst. However, there are some drawbacks to these commercial catalysts, including biological toxicity and low SCR performance below 300 °C, which limit their application in NH₃-SCR systems [1,4]. In recent years, the low-temperature NH₃-SCR technology, working downstream after the electrostatic precipitator, where most of the flue gas is cooled down and the SO₂/dusts are removed, has gained increasing attention [5,6].

Manganese-containing catalysts exhibit desirable catalytic activities at low temperatures, which received much attention in recent years [7–11]. However, Mn-based catalysts are easily deactivated when the treated flue gas contains SO₂. For this reason, the sulfur-poisoning mechanism of catalysts caused by SO₂ and SO₃ has been widely explored. The

active sites of catalysts were covered by ammonium bisulfate nitrate and metal sulfates deposited on the surface of catalysts, which potentially obstructed the SCR reaction at low temperatures [4,8,12]. Thus, fabricating Mn-based catalysts with both excellent catalytic activity and low SO₂ sensitivity at low temperatures has attracted great interest in recent years.

Researchers have suggested that the structure and morphology of catalysts in the low-temperature SCR process could enhance their SO₂ poisoning tolerance [13–15]. Recently, small-pore zeolites, such as SAPO-34, SSZ-13 and ZSM-5, have attracted more research owing to their exceptional catalytic activity and hydrothermal stability. Among them, SAPO-34 zeolite has a small eight-ring pore opening, a large CHA cavity and medium acidity, which has been extensively studied and used in NH₃-SCR reactions because of its desirable catalytic performance [16–19]. However, these microporous zeolites still have many weaknesses, including diffusion limitation of the pore/channel and reaction gas inhibition due to ammonium bisulfate (ABS) deposition, leading to catalyst deactivation in practical NH₃-SCR application. Hierarchical zeolites, which provide two or more levels of pore sizes, have attracted great attention. For example, Li et al. reported that 2.7 wt.% Cu/SAPO-34 with a hierarchical pore structure exhibited better SO₂ resistance compared to 2.7 wt.% Cu/SAPO-34 [20]. Liu et al. found that a 1.0-Cu/SAPO-34 catalyst synthesized by the one-step hydrothermal method exhibited superior catalytic activity at a temperature range of 140–430 °C [21]. Additionally, Guo et al. concluded that the decomposition rate of ABS on the SBA-15 catalyst with a larger average pore size was faster than that on conventional SBA-15 [22]. To the best of our knowledge, few studies have focused on the preparation and performance of the hierarchical MnO_x/SAPO-34 catalyst for low-temperature NH₃-SCR.

In this study, the hierarchical SAPO-34 zeolite was prepared by facile acid treatment with citric acid. The SAPO-34 zeolites etched by citric acid solutions with different concentrations were termed H-SAPO-34-*x* (*x* = 0.01, 0.1 and 0.125), in which *x* represents the molar concentration of the citric acid etching solution. The ethanol dispersion method was used to synthesize a series of MnO_x supported on hierarchical SAPO-34 catalysts. In addition, the low-temperature NH₃-SCR activities and SO₂ tolerance of the obtained catalysts were explored. Compared with the conventional MnO_x/SAPO-34 catalyst, the effect of the hierarchical pore structure on SCR activity and SO₂ resistance at low temperatures was investigated. The results indicate that hierarchical MnO_x/SAPO-34 catalysts exhibited excellent low-temperature SCR activity and SO₂ resistance. Among these hierarchical MnO_x/SAPO-34 catalysts (denoted as MnO_x/H-SAPO-34-*y*, *y* = 0.01, 0.1 and 0.125, in which *y* represents the molar concentration of the citric acid etching solution), MnO_x/H-SAPO-34-0.1 exhibited optimal low-temperature NH₃-SCR performance. Characterization analyses through XRD, SEM, TEM, FT-IR, Py-IR, NH₃-TPD, H₂-TPR, TG/DTG, XPS and BET demonstrated further exploration of the impact mechanisms of the hierarchical pore structure on SO₂ resistance, SCR activity and stability at low temperatures.

2. Results and Discussion

2.1. Catalyst Characterization

2.1.1. XRD

The ordered meso-structures and crystalline nature of catalysts were confirmed by low- and wide-angle XRD, respectively. As shown in Figure 1a, all the samples exhibited typical SAPO-34 characteristic diffraction peaks at 9.6°, 12.8°, 15.9° and 20.6° [23], and there were no impurity peaks before or after citric acid treatment. No manganese oxide characteristic diffraction peaks were observed in the XRD results for both MnO_x/H-SAPO-34-0.1 and MnO_x/SAPO-34, indicating that the Mn species were highly dispersed or persisted in an amorphous state within the catalysts. As shown in Figure 1b, there was a diffraction peak within in the range of 0.5°–1.0° for both samples, which can be assigned to the (111) reflections of an fcc structure (Fm3m), suggesting that a mesoporous structure was formed in SAPO-34 zeolites [24].

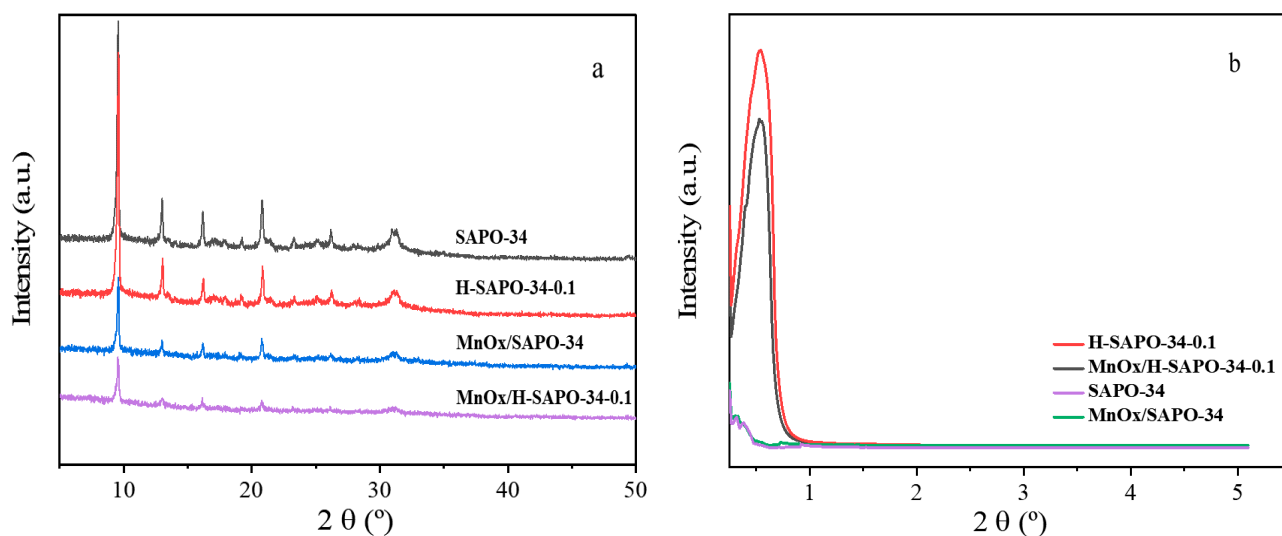


Figure 1. XRD patterns of SAPO-34, H-SAPO-34-0.1, (a) $\text{MnO}_x/\text{SAPO-34}$ and (b) $\text{MnO}_x/\text{H-SAPO-34-0.1}$ catalysts.

2.1.2. SEM and TEM

SEM was used to observe the morphological features of both the synthesized and reference zeolites (Figure 2). Cubic morphology of the characteristic CHA structure was observed in all samples. As the molar concentration of citric acid increased, the surface roughness of the SAPO-34 molecular sieve gradually increased. When the molar concentration of citric acid etching solution was 0.125 mol/L, the structure of the catalyst collapsed, which caused its external specific areas to decrease. Compared with SAPO-34, which displayed well-developed crystal faces, hierarchical SAPO-34 crystals showed a rough surface because of the surface etching with citric acid solution. As expected, the $\text{MnO}_x/\text{H-SAPO-34-0.1}$ zeolite retained its original structure well after loading manganese species, compared with the $\text{MnO}_x/\text{SAPO-34}$ sample. The fact that the $\text{MnO}_x/\text{H-SAPO-34-0.1}$ sample had much higher external specific surface areas than those of $\text{MnO}_x/\text{SAPO-34}$ prepared by conventional methods might be due to the special structure of the former. Figure 3 shows the EDS elemental mapping of the $\text{MnO}_x/\text{H-SAPO-34-0.1}$ catalyst. The elemental mapping results indicate that all elements, such as Al, Si, O, P and Mn species, were distributed homogeneously in the $\text{MnO}_x/\text{H-SAPO-34-0.1}$ catalyst. Consistent with the results of low-angle XRD, the TEM image for the $\text{MnO}_x/\text{H-SAPO-34-0.1}$ catalyst displayed in Figure 4 clearly shows that some mesopores were present within the sample. The HRTEM images (Figure 5) illustrate the lattice fringes of the $\text{MnO}_x/\text{H-SAPO-34-0.1}$ catalyst. The lattice fringe spacings of 0.311 and 0.383 nm shown in Figure 5a corresponded to the (111) plane of MnO_2 and the (211) plane of Mn_3O_4 , respectively, while the lattice fringe spacings of 0.690 and 0.272 nm shown in Figure 5b corresponded to the (110) plane of MnO_2 and the (222) plane of Mn_2O_3 , respectively. The most active crystal plane in the NH_3 -SCR reaction was considered to be the (110) plane of MnO_2 , which was highly dispersed in $\text{MnO}_x/\text{H-SAPO-34-0.1}$ [25]. This was one of the reasons for the high SCR activity of the $\text{MnO}_x/\text{H-SAPO-34-0.1}$ catalyst at low temperatures.

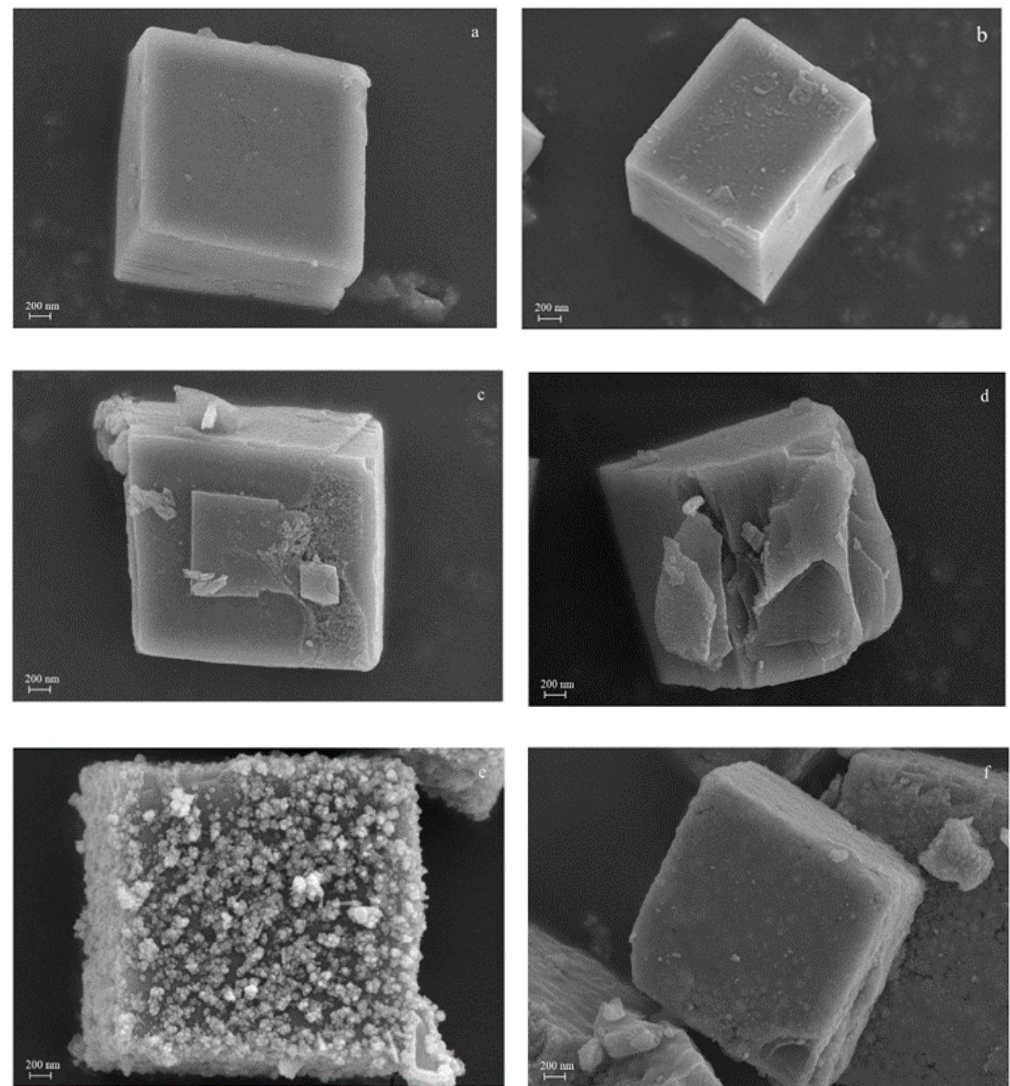


Figure 2. SEM patterns of SAPO-34 (a), H-SAPO-34-0.01 (b), H-SAPO-34-0.1 (c), H-SAPO-34-0.125 (d), MnO_x/SAPO-34 (e) and MnO_x/H-SAPO-34-0.1 (f).

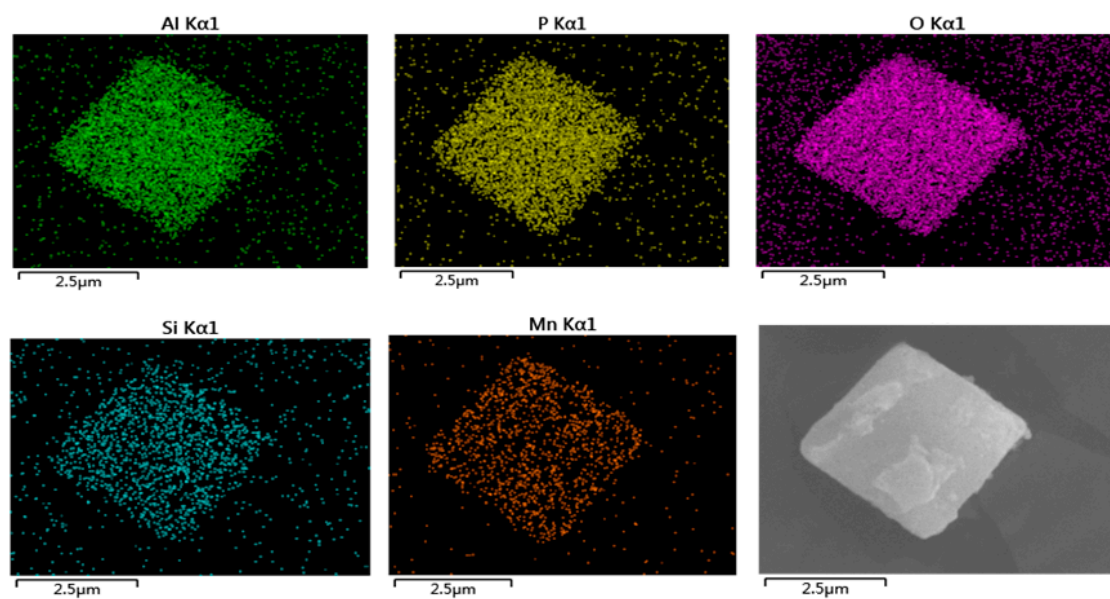


Figure 3. EDS mapping of MnO_x/H-SAPO-34-0.1 catalyst.

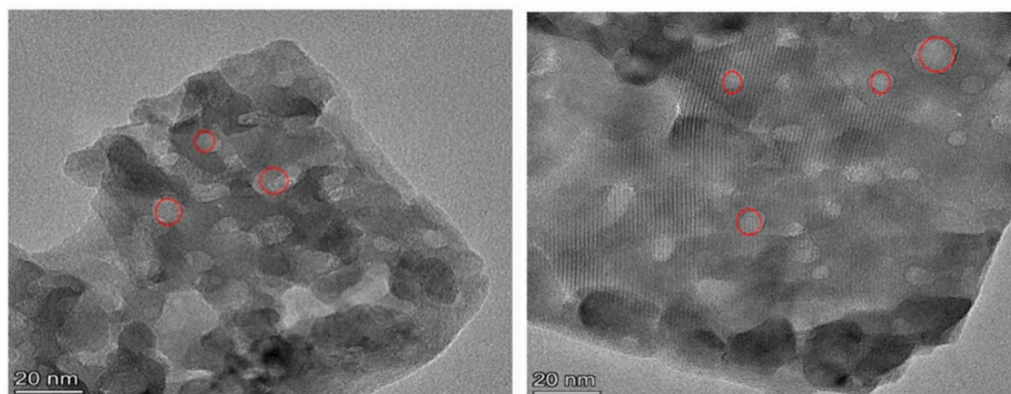


Figure 4. TEM patterns of $\text{MnO}_x/\text{H-SAPO-34-0.1}$ catalyst.

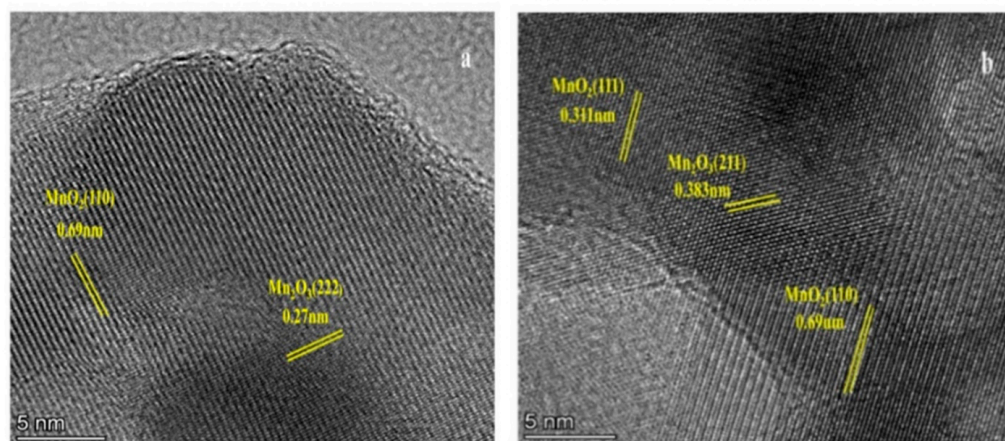


Figure 5. HRTEM patterns of $\text{MnO}_x/\text{H-SAPO-34-0.1}$ catalyst. (a) plane of MnO_2 and Mn_3O_4 (b) plane of MnO_2 and Mn_2O_3 .

2.1.3. BET

The N_2 adsorption–desorption isotherms and pore size distribution of all samples are shown in Figure 6. As seen in Figure 6a, $\text{MnO}_x/\text{SAPO-34}$ presented typical type I adsorption–desorption isotherms in the low-pressure regions ($P/P_0 < 0.01$). $\text{MnO}_x/\text{H-SAPO-34-0.1}$ exhibited a representative characteristic type IV isotherm and a well-defined hysteresis loop at the pressure regions of $0.4 < P/P_0 < 0.9$ [26]. Hysteresis loops could be observed in the region of $0.4 < P/P_0 < 0.9$ for sample $\text{MnO}_x/\text{H-SAPO-34-0.1}$, suggesting that there were secondary larger pores in the microporous structure of the SAPO-34 crystal [27]. The pore size distribution of samples in Figure 6b,c illustrates the existence of a mesopore structure with a pore size of approximately 5 nm. The results of the structural properties of the catalysts are listed in Table 1. Compared with conventional $\text{MnO}_x/\text{SAPO-34}$, it was worth noting that the specific surface areas of $\text{MnO}_x/\text{H-SAPO-34-0.1}$ increased from 248.9 to 428.26 m^2/g . Meanwhile, the external specific areas of $\text{MnO}_x/\text{H-SAPO-34-0.1}$ increased from 26.61 to 37.89 m^2/g compared to the conventional $\text{MnO}_x/\text{SAPO-34}$ catalyst. Significantly, with respect to SAPO-34 and $\text{MnO}_x/\text{SAPO-34}$, both H-SAPO-34-0.1 and $\text{MnO}_x/\text{H-SAPO-34-0.1}$ exhibited enhancements in mesopore volume and total pore volume, with a concomitant reduction in micropore volume. Combined with the SEM and TEM results, the BET results indicate that the hierarchical $\text{MnO}_x/\text{SAPO-34}$ catalysts were successfully synthesized.

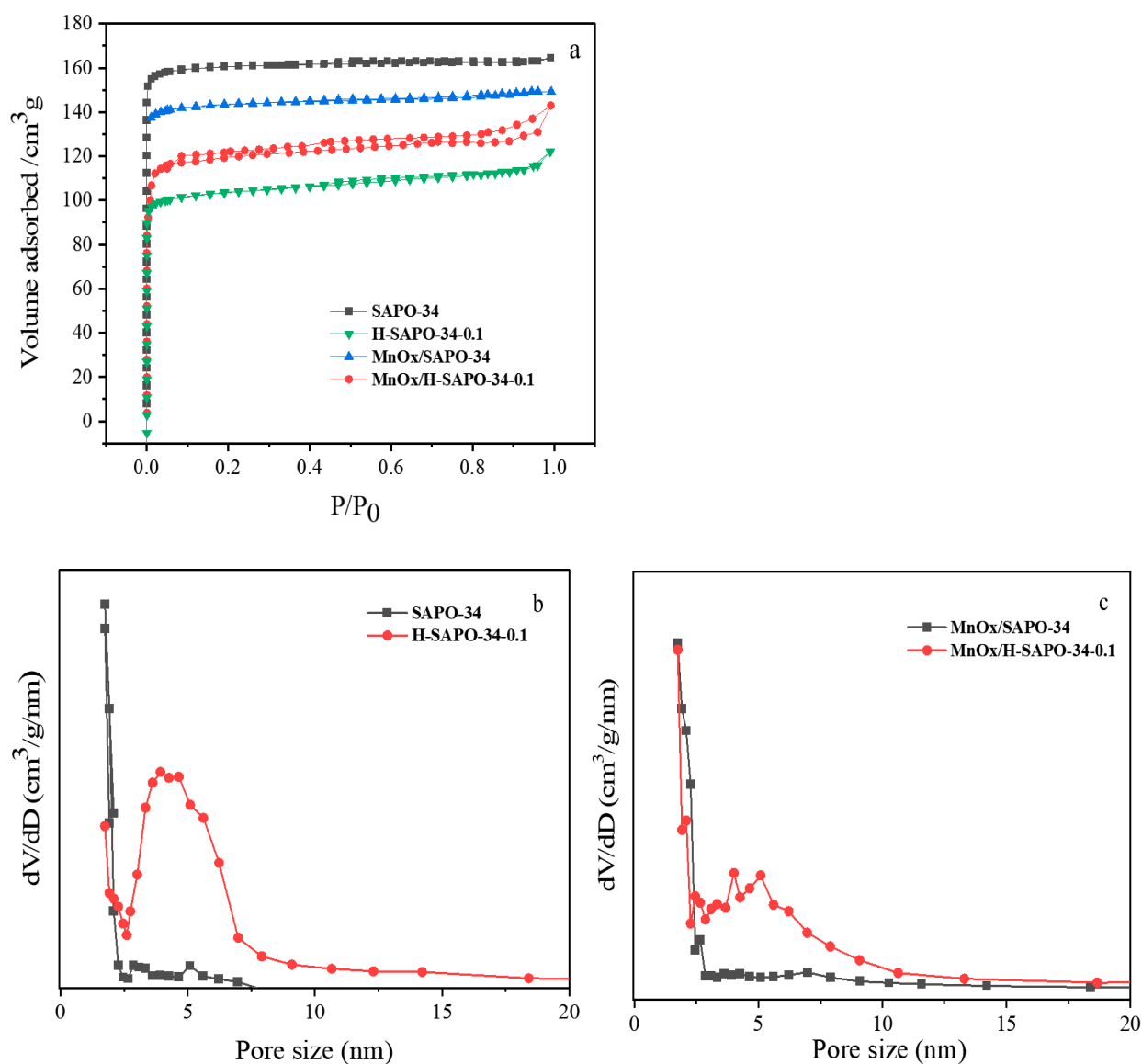


Figure 6. N_2 adsorption–desorption isotherms (a) and pore size distributions (b,c) of the synthesized catalysts.

Table 1. Structural properties of the samples.

Samples	$S_{BET}^a/$ ($m^2 \cdot g^{-1}$)	$S_{mic}^a/$ ($m^2 \cdot g^{-1}$)	$S_{ext}^a/$ ($m^2 \cdot g^{-1}$)	$V_{total}^b/$ ($cm^3 \cdot g^{-1}$)	$V_{micro}^b/$ ($cm^3 \cdot g^{-1}$)	$V_{meso}/$ ($cm^3 \cdot g^{-1}$)	Ave. D_{meso}^c (nm)
SAPO-34	489.90	444.04	25.86	0.212	0.212	-	-
H-SAPO-34-0.1	548.80	510.24	38.56	0.253	0.211	0.042	5.19
MnO _x /SAPO-34	248.91	222.29	26.61	0.131	0.131	-	-
MnO _x /H-SAPO-34-0.1	428.26	390.37	37.89	0.222	0.177	0.045	5.22

^a Calculated by BET method. ^b Calculated by t-plot method. ^c Calculated by BJH method.

2.1.4. FT-IR

The chemical states of fresh and deactivated catalysts were studied by FT-IR spectroscopy and the results are illustrated in Figure 7. The sulfated MnO_x/SAPO-34 and MnO_x/H-SAPO-34-0.1 samples were marked as MnO_x/SAPO-34-S and MnO_x/H-SAPO-34-0.1-S, respectively. All of the catalysts displayed vibration absorptions centering at wave numbers of 1042 cm^{-1} . This was mainly due to the asymmetric stretching of the Si-O-Si bond. The bands at around 1640 and 3314 cm^{-1} were caused by the stretching vibrations

of H-OH and O-H bonds from H₂O, respectively [28]. When the MnO_x/SAPO-34 and MnO_x/H-SAPO-34-0.1 were exposed to SO₂ atmosphere, both of them showed a spectrum roughly similar to that of the fresh catalysts. However, one new peak appeared at 1420 cm⁻¹, which could be assigned to NH₄⁺ species chemisorbed on Brønsted acid sites. This implied that after the sulfur resistance test, ammonium species were formed on the surface of the catalyst. Concurrently, a new weak band appeared at 525 cm⁻¹, which might be assigned to the characteristic frequencies of the SO₄²⁻ [29]. These findings indicate that sulfate species may form during the SCR reaction in the presence of SO₂ by binding to metal oxides or adsorbed NH₃ species. From the above results, the bands at 1420 and 525 cm⁻¹ were clearly visible for MnO_x/SAPO-34 after the sulfur resistance test. However, these significant peaks were not obvious in the spectrum of MnO_x/H-SAPO-34-0.1, indicating that sulfate species were only slightly deposited on this sample.

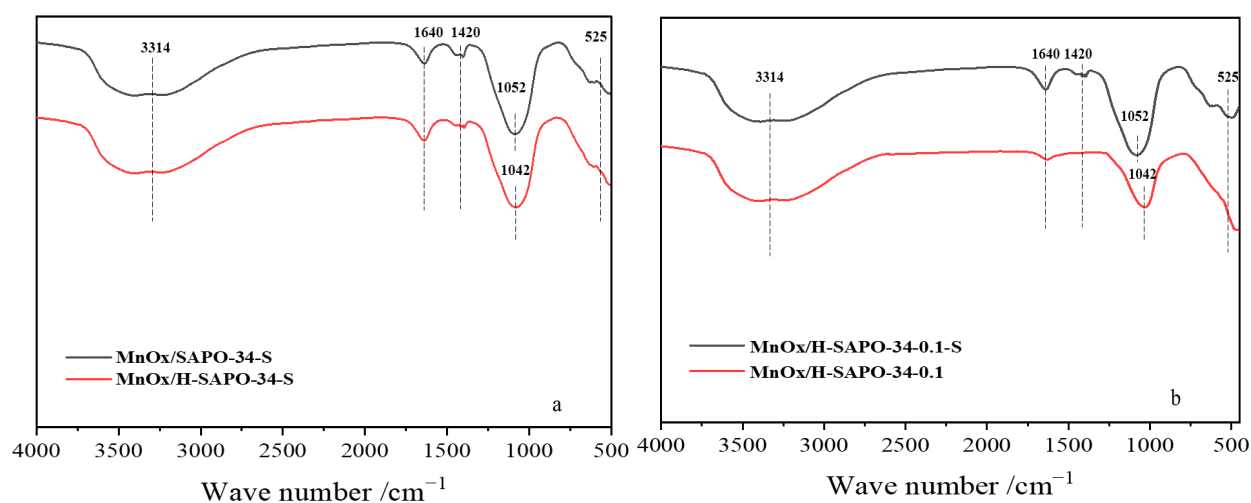


Figure 7. FT-IR spectrum of the fresh and deactivated MnO_x/SAPO-34 (a) and MnO_x/H-SAPO-34-0.1 (b) catalysts.

2.1.5. NH₃-TPD and Py-IR

NH₃-TPD experiments were conducted to probe the surface acid properties of both hierarchical and conventional MnO_x/SAPO-34 catalysts. As shown in Figure 8a and Table 2, the catalysts exhibited two desorption peaks in the whole temperature range. The peak from 170 to 220 °C was likely due to NH₃ adsorbed on physical and weak acid sites. The desorption peak at 380–530 °C was assigned to NH₃ adsorbed on the strong acid sites [30]. The strong acid amount of the hierarchical MnO_x/H-SAPO-34-0.1 was the highest among the samples, which suggests that the larger pore structure and higher surface area enhanced the concentration and acidity of strong acid sites. Therefore, the hierarchical MnO_x/SAPO-34 catalysts with larger specific surface areas, which could provide more strong acid sites on the surface of the catalysts for the adsorption and activation of NH₃, exhibited the optimal NH₃-SCR performance at low temperatures. Pyridine is larger than the eight-ring diameter of the CHA structure. The IR spectra of adsorbed pyridine was therefore related to the acid site in the mesopore channels [31]. The Py-IR measurement defined and established the types of acid sites in Figure 8b. Furthermore, the amounts of total and medium strong acid over the MnO_x/SAPO-34 catalysts were acquired with the number of desorbed pyridine molecules at 200 °C. Brønsted acid (B) and Lewis acid (L) were found to be present on both MnO_x/SAPO-34 and MnO_x/H-SAPO-34-x, corresponding to the bands at around 1535 and 1445 cm⁻¹, respectively. In addition, the peak at around 1490 cm⁻¹ was assigned to both Brønsted and Lewis acid sites. As shown in Figure 8b, the Lewis acid sites were the main acid sites of the as-obtained catalysts, and there was also a small number of Brønsted acid sites. With the increase in the concentration of citric acid etching solution, the number of Brønsted acid sites increased gradually. In addition, the

MnO_x/H-SAPO-34-0.1 catalyst had the highest B/L ratio (0.65) among all of the catalysts, which was favorable for the oxidation of NO to NO₂ for the reaction of NO + NH₃ + O₂.

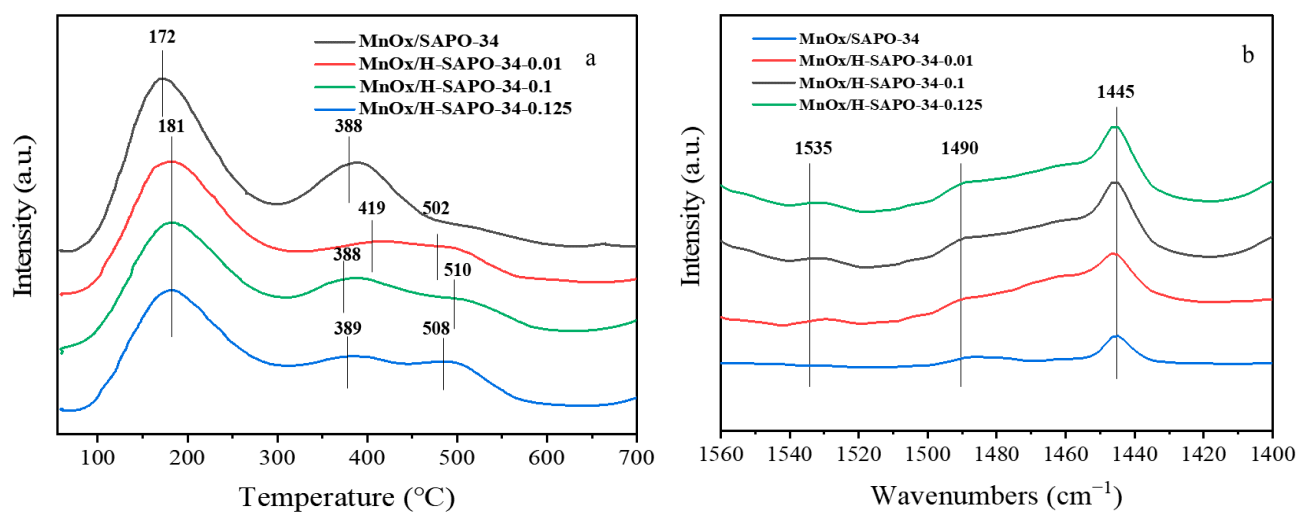


Figure 8. NH₃-TPD (a) and Py-IR (b) profiles on MnO_x/SAPO-34 and hierarchical MnO_x/SAPO-34 catalysts.

Table 2. Acidity data of MnO_x/SAPO-34 and hierarchical MnO_x/SAPO-34.

Sample	Amount of Acid Sites (mmol/g) ^a		Amount of Acid Sites (umol/g) ^b		B/L	Total Acidity (mmol/g)
	Weak	Strong	Lewis Acid Sites	Brønsted Acid Sites		
MnO _x /SAPO-34	0.771	0.316	70.22	29.78	0.42	1.098
MnO _x /H-SAPO-34-0.01	0.593	0.327	65.96	34.04	0.52	0.899
MnO _x /H-SAPO-34-0.1	0.537	0.377	60.75	39.25	0.65	0.914
MnO _x /H-SAPO-34-0.125	0.534	0.336	61.60	38.4	0.62	0.873

^a NH₃-TPD method. ^b Py-IR method.

SO₂ produced sulfur ammonium salt, which could cover and occupy some active sites and had a serious influence on the strong acidity of the catalysts. As seen in Figure 8, the MnO_x/H-SAPO-34-0.1 sample had a higher amount of strong acid sites and Brønsted acid sites than the MnO_x/SAPO-34 sample. This discovery indicates that the hierarchical pore structure could effectively inhibit the sulfation of active sites and provide more acid sites for the adsorption of NH₃ on the surface of the catalyst, which was in accordance with the results of the SO₂ resistance test.

2.1.6. H₂-TPR

H₂-TPR characterization was performed to investigate the redox properties of the catalysts, and the corresponding H₂-TPR profiles are shown in Figure 9. Both MnO_x/H-SAPO-34-0.1 and MnO_x/SAPO-34 catalysts presented two reduction peaks in the range of 200–800 °C. For the profile of MnO_x/SAPO-34, the peaks at 416 and 513 °C could be assigned to MnO₂/Mn₂O₃ → Mn₃O₄ and Mn₃O₄ → MnO, respectively [32]. Compared with the conventional MnO_x/SAPO-34 catalyst, it is clear that the reduction peaks shifted to a lower temperature centering at 351 and 453 °C, suggesting that the reducibility of MnO_x/H-SAPO-34-0.1 highly increased. Based on previous studies, the reduction peak area had a direct relationship with the consumed content of H₂ [33]. It can be seen that the reduction peak area of MnO_x/H-SAPO-34-0.1 that appeared at relatively low temperature was much larger than that of MnO_x/SAPO-34, suggesting that the manganese species on

the $\text{MnO}_x/\text{H-SAPO-34-0.1}$ surface is highly dispersed, which is consistent with the results of the EDS mapping [34]. In addition, the Mn species with high valence states such as Mn^{4+} and Mn^{3+} , which were conducive to the adsorption of NH_3 and NO to form $\text{Mn}^{4+}\text{-NH}_3$ and $\text{Mn}^{3+}\text{-NO}_3$, could enhance the catalytic activity in the $\text{NH}_3\text{-SCR}$ reaction [35]. Therefore, the $\text{MnO}_x/\text{H-SAPO-34-0.1}$ catalyst with higher reducibility exhibited optimal low-temperature performance.

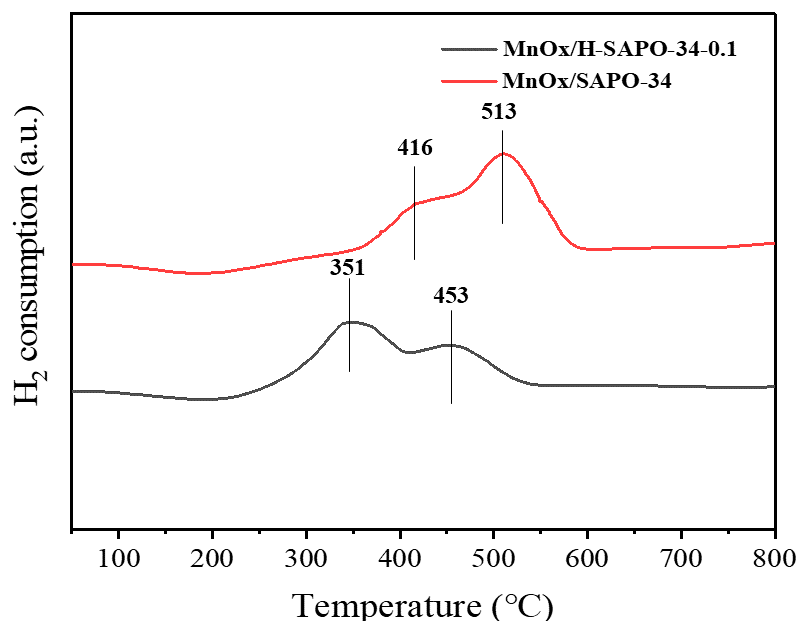


Figure 9. H_2 -TPR profiles of $\text{MnO}_x/\text{SAPO-34}$ and $\text{MnO}_x/\text{H-SAPO-34-0.1}$ catalysts.

2.1.7. XPS

XPS characterization was performed to investigate the atomic distribution and composition of manganese, sulfur and oxygen ions on fresh and deactivated catalysts. The $\text{Mn } 2p_{3/2}$, $\text{O } 1s$ and $\text{S } 2p$ photoelectron spectra are shown in Figure 10 and the assignments of the characteristic peaks in the XPS results of fresh and deactivated catalysts are listed in Table 3a. XPS-peak 4.1 software was used to perform the XPS peak fitting and background subtraction. By performing a peak fitting deconvolution, the $\text{Mn } 2p_{3/2}$ spectra were divided into three peaks, Mn^{2+} (640.8 ± 0.3)eV, Mn^{3+} (641.8 ± 0.2)eV and Mn^{4+} (643.1 ± 0.5)eV [35,36]. $\text{O } 1s$ spectra were separated into three characteristic peaks, which were ascribed to lattice oxygen species (O^{2-} marked as O_α) at (529.8 ± 0.2)eV, chemisorbed oxygen species (O_2^- or O^- marked as O_β), including surface adsorbed oxygen and that of hydroxyl-like groups at (532.1 ± 0.2)eV and surface hydroxyl species/adsorbed water molecules (OH or H_2O marked as O_γ) at (534.5 ± 0.2)eV [37,38]. In addition, the $\text{S } 2p$ spectra can be detected in the deactivated samples (Figure 10c). The peaks at (169.7 ± 0.2)eV and (168.6 ± 0.2)eV are attributed to $\text{S}^{6+}/\text{S}^{4+} 2p_{3/2}$ and $2p_{1/2}$, respectively. Thus, it can be concluded that both SO_4^{2-} and SO_3^{2-} were generated on the surface of catalysts in the $\text{NH}_3\text{-SCR}$ reaction with the appearance of SO_2 [39–44].

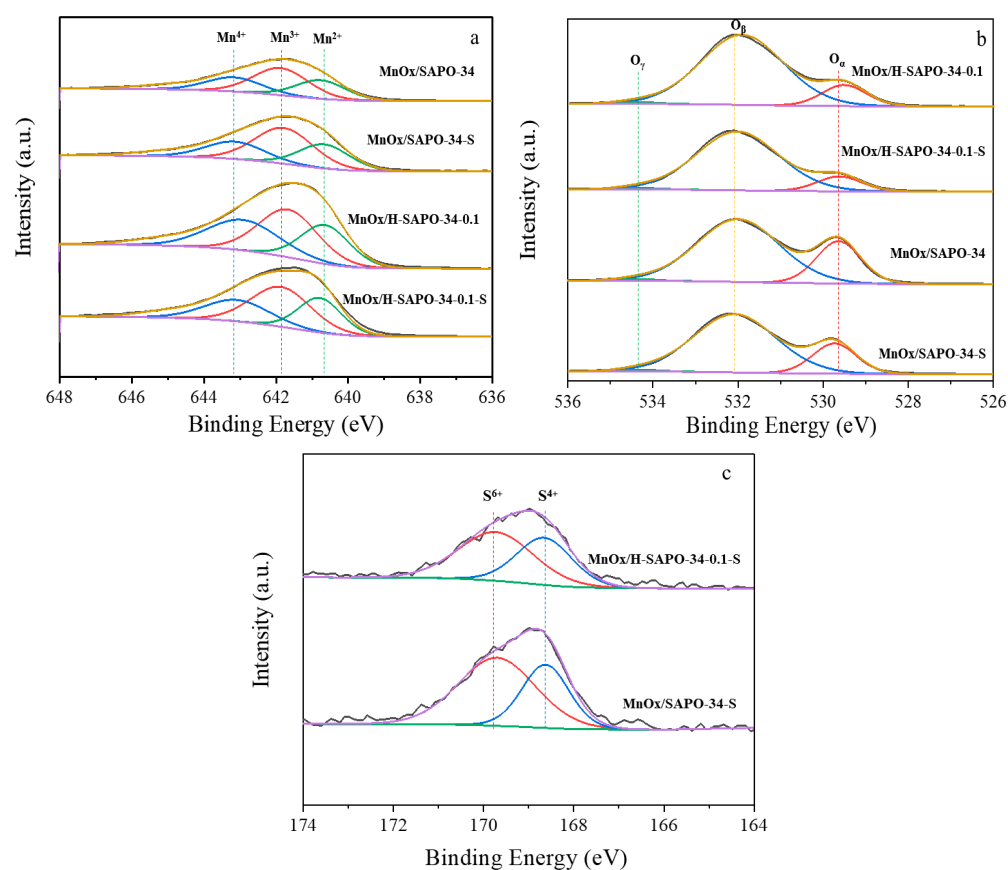


Figure 10. High-resolution XPS spectra of all samples: (a) Mn $2p_{3/2}$, (b) O $1s$, (c) S $2p$.

Table 3. (a) Assignments of the characteristic peaks in XPS results of fresh and deactivated catalysts.

Element	Binding Energy/eV	Assignment	FWHM/eV
O $1s$	529.6–530.0	lattice oxygen species	1.28
	531.9–532.3	chemisorbed oxygen species	2.39
	534.3–534.7	surface hydroxyl species/adsorbed water molecules	1.20
Mn $2p_{3/2}$	640.5–641.1	Mn $^{2+}$	1.98
	641.6–642.0	Mn $^{3+}$	2.21
	642.6–643.6	Mn $^{4+}$	1.67
S $2p$	169.5–169.9	S $^{6+}$	2.01
	168.4–168.8	S $^{4+}$	1.22

(b) Surface compositions of all samples by XPS analysis.

Sample	Atomic Fraction (%)			X_S (%)	X_O (%)			X_{Mn} (%)			$X(Mn^{3+} + Mn^{4+}) / X(Mn^{3+} + Mn^{2+} + Mn^{4+})$ (%)
	Mn	O	Others ^a		S	O_α	O_β	O_γ	Mn $^{2+}$	Mn $^{3+}$	
MnO $_x$ /SAPO-34	7.87	59.12	40.88	-	26.26	72.69	1.05	28.88	46.46	24.66	71.12
MnO $_x$ /SAPO-34-S	6.07	62.86	28.92	2.15	21.26	77.44	1.30	30.87	43.70	25.43	69.13
MnO $_x$ /H-SAPO-34-0.1	13.96	59.8	26.24	-	13.69	84.98	1.33	27.55	40.74	31.71	72.45
MnO $_x$ /H-SAPO-34-0.1-S	11.30	59.51	27.88	1.31	11.82	86.17	2.01	28.05	48.30	23.65	71.95

Others^a: Si, Al, P, O.

The results of surface compositions of all samples are shown in Table 3b. It was found that MnO_x/H-SAPO-34-0.1 (72.45) had a higher (Mn³⁺ + Mn⁴⁺)/(Mn³⁺ + Mn²⁺ + Mn⁴⁺) ratio than that of MnO_x/SAPO-34 (71.12), which is consistent with the results of H₂-TPR. The ratios of (Mn³⁺ + Mn⁴⁺)/(Mn³⁺ + Mn²⁺ + Mn⁴⁺) for MnO_x/H-SAPO-34-0.1 and MnO_x/SAPO-34 decreased from 72.45% to 71.95% and from 71.12% to 69.13% after sulfation, respectively. However, this ratio over sulfated MnO_x/H-SAPO-34-0.1 stayed at a high level, even higher than that over fresh MnO_x/SAPO-34. It has been indicated that Mn⁴⁺ species and their redox processes promoted the catalytic cycle of NH₃-SCR of NO_x at low temperatures [37,45]. Therefore, MnO_x/H-SAPO-34-0.1 exhibited excellent low-temperature activity and high tolerance to SO₂.

Furthermore, compared with MnO_x/SAPO-34 (72.69), MnO_x/H-SAPO-34-0.1 (84.98) had a higher ratio of O_β/(O_α + O_β). It has been reported that higher percentages of O_β promoted the catalytic cycle of NH₃-SCR of NO_x [46]. Therefore, the morphological features of MnO_x/H-SAPO-34-0.1 indicate that the hierarchical pore structure could produce extra surface vacancies to activate oxygen [33]. The hierarchical pore structure appeared to facilitate the transformation of NO to NO₂, which improved the SCR performance at low temperatures. It is worth noting that the atomic ratio of S in the deactivated MnO_x/SAPO-34 catalyst was slightly higher than that in the deactivated MnO_x/H-SAPO-34-0.1 sample, indicating that the sulfates did not accumulate in large quantities on the surface of the MnO_x/H-SAPO-34-0.1-S sample, which is in keeping with the results of FT-IR. It has been reported that the deposition of ABS and the sulfurating of active component Mn were the main causes of catalyst deactivation [47]. Therefore, the hierarchical pore structure can attain a dynamic balance between the formation and decomposition of ammonium sulfate, which could provide an increased surface area for the reaction process and prolong the retention of reactants on the catalyst surface. Moreover, the special structure decreased the possibility of surface active sites being taken up by SO₂ and prevented the formation of sulfates from blocking the active sites, leading to a high SO₂ resistance [48].

2.1.8. TG/DTG

In order to explore the SO₂ resistance of MnO_x/H-SAPO-34-0.1 and MnO_x/SAPO-34 catalysts, TG experiments were performed. The results are shown in Figure 11. As seen in Figure 11a, three weight losses are shown in the TG curves in the tested range. The weight loss below 200 °C was likely due to the evaporation of absorbed water, whereas the weight loss (A) between 200 and 450 °C was caused by the decomposition of ABS, and the latter weight loss (B) at 700–850 °C corresponded to the decomposition of MnSO₄ [44]. To investigate the possible pore size effect, a decomposition experiment was also performed on the MnO_x/H-SAPO-34-0.1 sample. The results are shown in Figure 11b. It was found that the TG signals of MnO_x/H-SAPO-34-0.1 displayed similar trends to those of MnO_x/SAPO-34. However, the weight loss (A) of MnO_x/SAPO-34 and MnO_x/H-SAPO-34-0.1 was measured at 4.05% and 3.39%, respectively. Smaller weight loss (A) was observed in MnO_x/H-SAPO-34-0.1, indicating that less ABS formed on the sample, which was consistent with the XPS results. Meanwhile, the weight loss (B) of MnO_x/SAPO-34 and MnO_x/H-SAPO-34-0.1 was measured at 2.12% and 1.73%, respectively. The results of BET and NH₃-TPD suggest that the MnO_x/H-SAPO-34-0.1 catalyst with a larger specific surface area along with abundant acid sites, which could offer a high-efficiency place to trigger the SCR reaction, resulted in improved SO₂ tolerance [49]. The TG/DTG analysis indicated that fewer sulfates were deposited on the surface of the MnO_x/H-SAPO-34-0.1 catalyst, which provided evidence for the anti-SO₂ capability of the hierarchical pore structure. Consistent with the results of NH₃-TPD and Py-IR, the effect of the hierarchical pore structure was to make a balance between effective acid sites and the formation/decomposition of ABS, thus enhancing the deNO_x properties and suppressing the blocking effect of SO₂. Consequently, these phenomena suggest that the hierarchical pore structure promoted the diffusion of the reaction gas and minimized the sulfur poisoning of active Mn sites. This finding is

consistent with the results obtained with regard to the sulfur poisoning resistance of the $\text{MnO}_x/\text{H-SAPO-34-0.1}$ catalyst.

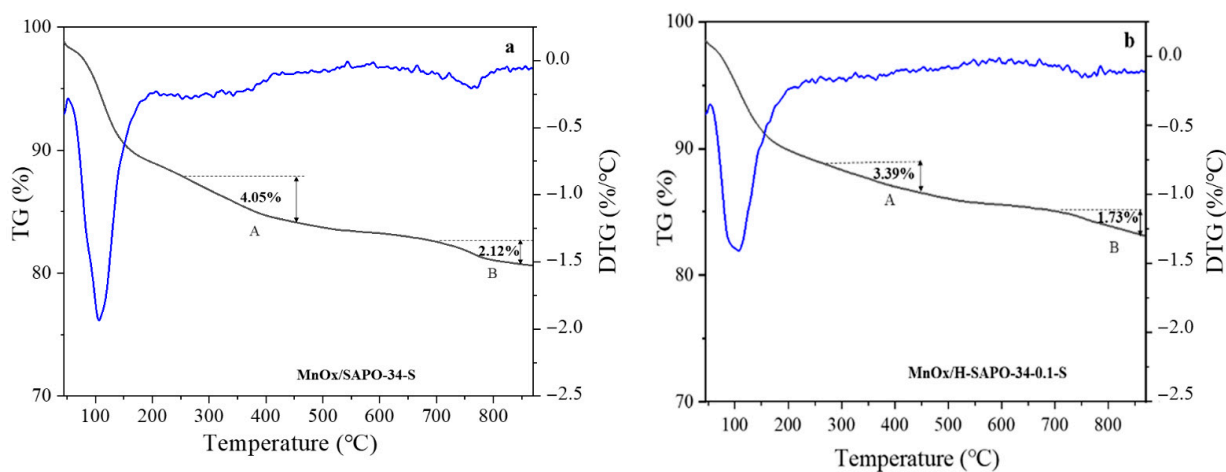


Figure 11. TG-DTG patterns of sulfated $\text{MnO}_x/\text{SAPO-34}$ (a) and $\text{MnO}_x/\text{H-SAPO-34-0.1}$ (b) catalysts.

2.2. Catalytic Performance of the Low-Temperature $\text{NH}_3\text{-SCR}$

2.2.1. Catalytic Activity Tests

As shown in Figure 12, performances of the hierarchical $\text{MnO}_x/\text{SAPO-34}$ and $\text{MnO}_x/\text{SAPO-34}$ catalysts during the $\text{NH}_3\text{-SCR}$ reaction were evaluated in the temperature range of 80–240 °C. To explore the influence of the hierarchical pore structure on the $\text{NH}_3\text{-SCR}$ reaction, the NO conversion over $\text{MnO}_x/\text{SAPO-34}$ was measured for comparison. The $\text{MnO}_x/\text{SAPO-34}$ showed little activity until the temperature reached 120 °C, and the NO conversion gradually increased to the maximum value (about 90%) at 180 °C. At low temperatures, hierarchical $\text{MnO}_x/\text{SAPO-34}$ catalysts performed better than $\text{MnO}_x/\text{SAPO-34}$. The NO conversion with different hierarchical $\text{MnO}_x/\text{H-SAPO-34}$ catalysts as a function of the molar concentration of the citric acid etching solution in the $\text{NH}_3\text{-SCR}$ reaction is shown in Figure 12. Among the hierarchical $\text{MnO}_x/\text{SAPO-34}$ catalysts, the $\text{MnO}_x/\text{H-SAPO-34-0.1}$ catalyst exhibited the optimal NO conversion of 95% with an N_2 selectivity over 90% in the temperature range of 80–240 °C. The superior $\text{NH}_3\text{-SCR}$ performance obtained with $\text{MnO}_x/\text{H-SAPO-34-0.1}$ may due to the intercalation of mesoporous structures, which provided more channels and could substantially promote the mass transfer of reactants or products at low temperatures.

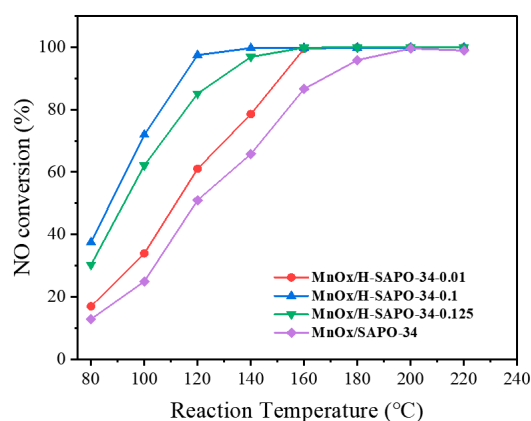


Figure 12. SCR activity of $\text{MnO}_x/\text{H-SAPO-34-0.01}$, $\text{MnO}_x/\text{H-SAPO-34-0.1}$, $\text{MnO}_x/\text{H-SAPO-34-0.125}$ and $\text{MnO}_x/\text{SAPO-34}$ catalysts.

2.2.2. Impact of SO₂ on Catalytic Activity

The effect of SO₂ on the catalytic performance of MnO_x/SAPO-34 and MnO_x/H-SAPO-34-0.1 catalysts was investigated at 120 °C. As shown in Figure 13, when 100 ppm SO₂ was added into the feed gas, a drop in NO conversion of approximately 80% occurred over MnO_x/SAPO-34. After removing the SO₂, the NO conversion did not fully recover. Nevertheless, the NO conversion of MnO_x/H-SAPO-34-0.1 was still maintained at 100% after the 40-min test. The MnO_x/SAPO-34 catalyst showed a relatively faster deactivation in a short period of time, indicating a notable difference in reaction efficiency. The SCR performance of MnO_x/H-SAPO-34-0.1 decreased slowly and remained above 65% for the next 200 min. Pan et al. concluded that competitive adsorption between reactant molecules and toxicants on the surface of the catalyst may promote the deactivation of the catalyst [50]. Compared to traditional MnO_x/SAPO-34 catalysts, the MnO_x/H-SAPO-34-0.1 catalyst's hierarchical pore structure was therefore found to be a key factor contributing to its high SO₂ poisoning resistance. The hierarchical pore structure might inhibit ammonium bisulfate aggregation and facilitate dispersion of the active phase.

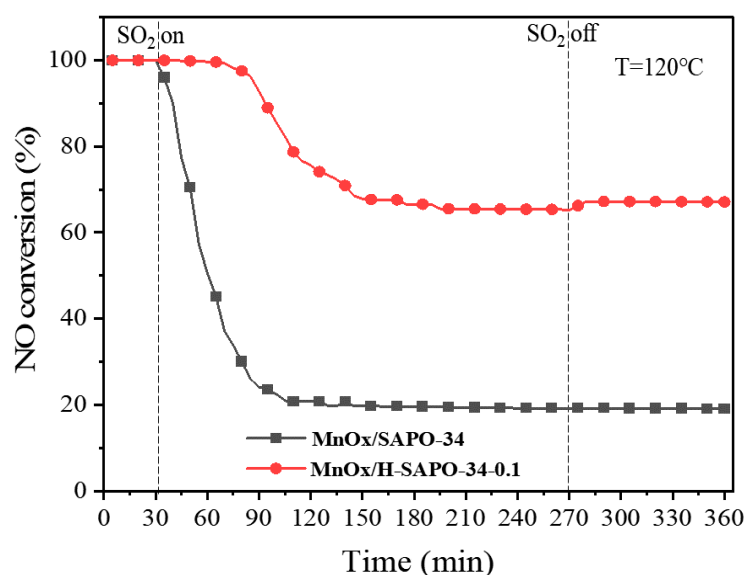


Figure 13. SO₂ tolerance of MnO_x/SAPO-34 and Mn/H-SAPO-34-0.1 in NH₃-SCR reaction.

Reaction conditions: 800 ppm NH₃, 800 ppm NO, 100 ppm SO₂ (when needed), 5 vol.% O₂, Ar to balance, T = 120 °C, gas hourly space velocity (GHSV) = 40,000 h⁻¹.

3. Materials and Methods

3.1. Catalysts Preparation

3.1.1. Preparation of Hierarchical SAPO-34

The SAPO-34 zeolite with a hierarchical pore structure (H-SAPO-34) was obtained by efficient post-synthesis via citric acid etching based on previous studies [31]. The carrier catalyst in this study was a commercial SAPO-34 with a Si/Al mass ratio of 0.27 (XFNANO Company, Nanjing, China). Typically, a certain amount of citric acid (Aladdin, Shanghai, China) was dissolved in 100 mL of ethanol and stirred for 30 min at room temperature. An amount of 3 g SAPO-34 was then added to the solution with vigorous stirring for 30 min. Then, the solution was transferred into an oil bath at 90 °C for 6 h. The product was washed with deionized water, filtered and dried overnight at 110 °C. The as-synthesized products were calcined at 550 °C for 5 h to obtain H-SAPO-34. The SAPO-34 zeolites etched in citric acid solutions with different concentrations were termed H-SAPO-34-x (x = 0.01, 0.1 and 0.125), in which x represents the molar concentration of the citric acid etching solution.

3.1.2. Preparation of the Catalysts

The ethanol dispersion method was used to prepare MnO_x/SAPO-34 catalysts with a hierarchical pore structure. Manganese nitrate (50% by weight in H₂O, Aladdin, Shanghai, China) was used as a precursor. The mass fraction of manganese was 15% and 2.72 mL of 50 wt.% Mn(NO₃)₂ was dissolved in 50 mL ethanol and stirred at ambient temperature. An amount of 3g H-SAPO-34-x was then added while being stirred. The solution was treated with ultrasound for 30 min and stirred continuously at 80 °C until the solvent evaporated completely. The products were dried at 100 °C and calcined at 400 °C for 4 h. The synthesized catalysts were denoted as MnO_x/H-SAPO-34-y (y = 0.01, 0.1 and 0.125, where y is the molar concentration of the citric acid etching solution). The ordinary MnO_x/SAPO-34 catalyst was prepared following the same method for comparison.

3.2. Catalysts Characterization

X-ray powder diffraction (XRD) measurement in the 2θ range of 0°–50° was obtained with the SmartLab (3KW) Japan Rigaku (Tokyo, Japan) X-ray diffractometer D8 using Cu Kα radiation (λ = 1.5418 Å). The scanning step size was 0.02°·s⁻¹. The distribution of Mn, Si, Al, P and O species was observed using a field emission SEM in JEOL JSM-6700F (Tokyo, Japan) with X-ray energy-dispersive spectrometry (EDS). The micro-structural characterization by transmission electron microscope (TEM) images was determined by JEM-2010 (JEOL, Tokyo, Japan) with a working voltage of 200 KV. BET specific surface area and pore characterization were tested using the N₂ adsorption–desorption on an ASAP 2020 (Drive Norcross, GA, USA) analyzer at –195 °C. X-ray photoelectron spectroscopy (XPS) was performed through the spectrum (K-Alpha⁺ ULTRA DLD) equipped with an Al Kα (1487 eV) radiation source.

Thermogravimetry (TG) was conducted using a STA449C-QMS403 thermal analyzer (Netisch, Germany) at a temperature range of 200–900 °C, with a heating rate of 10 °C min⁻¹ in 5% O₂/Ar. A Thermo Nicolet iS50 Spectrometer with a resolution of 4 cm⁻¹ was used to measure the FT-IR spectra of catalysts. NH₃ temperature-programmed desorption (NH₃-TPD) experiments were conducted on the Tp-5080 (Xianquan Industrial and Trading Co., Ltd., Tianjin, China). To explore pyridine adsorption, the sample was dehydrated at 450°C under a dynamic vacuum (1.5 × 10⁻³ Pa), followed by saturated adsorption of pyridine at room temperature. Py-IR spectra were then evacuated at 200 °C. H₂-TPR was conducted using a Tp-5080 (Xianqua, China) at a temperature range of 0–800 °C.

3.3. Catalysts Evaluation

A fixed-bed quartz flow reactor at atmospheric pressure was used to carry out SCR activity tests for the catalysts. The reaction temperature was increased from 25 to 240 °C at a rate of 5 °C/min, with an isotherm step of 20 °C. An amount of 800 mg of 40–60 mesh catalysts was used in each test. The simulated gas was composed of 800 ppm NH₃, 800 ppm NO, 5.0% O₂ and 100 ppm SO₂ (when needed) and balanced by Ar. All of the tests were performed with a total flow rate of 600 mL/min and a gas hourly space velocity (GHSV) of 40,000 h⁻¹. A NO-NO₂-NO_x analyzer (Thermal Scientific, model 42i-HL, Waltham, MA, USA) was used to measure the concentrations of NO and NO₂. The conversion of NO was calculated by

$$C_{\text{NO}} = (1 - [\text{NO}]_{\text{outlet}}/[\text{NO}]_{\text{inlet}}) \times 100\% \quad (1)$$

where [NO]_{inlet} refers to the concentration of the NO inlet gas and [NO]_{outlet} refers to the concentration of the NO outlet gas.

4. Conclusions

In this work, citric acid treatment was used to synthesize a series of hierarchical MnO_x/SAPO-34 catalysts. It was found that the hierarchical pore structure improved the low-temperature activity and SO₂ resistance of the MnO_x/SAPO-34 catalyst. Among them, MnO_x/H-SAPO-34-0.1 presented the optimal SCR performance with more than 90% NO

conversion at 110–240 °C. Moreover, the impact of introducing SO₂ to MnO_x/H-SAPO-34-0.1 on NO conversion was lesser than that observed in the MnO_x/SAPO-34 catalyst. Numerous characterizations demonstrated that the hierarchical pore structure significantly increased the BET surface area and Mn⁴⁺ percentage as well as the acid site quantity of the MnO_x/SAPO-34 zeolite, all of which were responsible for improving the SCR activity at low temperatures. The results of TG/DTG showed that fewer manganese sulfate species and ABS formed on the surface of the MnO_x/H-SAPO-34-0.1-S catalyst. The XPS results indicated that the MnO_x/H-SAPO-34-0.1 catalyst retained a high ratio of Mn oxides with a high valence state after sulfation. These phenomena could be ascribed to the fact that the hierarchical pore structure facilitated the decomposition of surface sulphates deposited on the catalyst during the SCR reaction, thus effectively reducing the SO₂ poisoning of active Mn sites. Overall, the low-temperature SCR activity and SO₂ tolerance of the MnO_x/SAPO-34 zeolite were significantly improved by the hierarchical pore structure, which could supply a rational strategy for the further design of Mn-based SCR catalysts.

Author Contributions: Writing, original draft preparation, L.Z.; writing, review and editing, L.Z., J.G. and C.Y.; funding acquisition, B.H.; supervision, B.H. All authors have read and agreed to the published version of the manuscript.

Funding: The project is financially supported by the National Natural Science Foundation of China (NSFC-51478191) and the Key Research and Development Plan of Guangdong Province (2019B110207001).

Conflicts of Interest: The authors declare no conflict of interest.

References

1. Busca, G.; Lietti, L.; Ramis, G.; Berti, F. Chemical and mechanistic aspects of the selective catalytic reduction of NO_x by ammonia over oxide catalysts: A review. *Appl. Catal. B Environ.* **1998**, *18*, 1–36. [[CrossRef](#)]
2. Zhang, T.; Chang, H.; Li, K.; Peng, Y.; Li, X.; Li, J. Different exposed facets VO_x/CeO₂ catalysts for the selective catalytic reduction of NO with NH₃. *Chem. Eng. J.* **2018**, *349*, 184–191. [[CrossRef](#)]
3. Xie, L.; Liu, F.; Ren, L.; Shi, X.; Xiao, F.-S.; He, H. Excellent Performance of One-Pot Synthesized Cu-SSZ-13 Catalyst for the Selective Catalytic Reduction of NO_x with NH₃. *Environ. Sci. Technol.* **2014**, *48*, 566–572. [[CrossRef](#)]
4. Li, J.; Chang, H.; Ma, L.; Hao, J.; Yang, R.T. Low-temperature selective catalytic reduction of NO_x with NH₃ over metal oxide and zeolite catalysts—A review. *Catal. Today* **2011**, *175*, 147–156. [[CrossRef](#)]
5. Hammershoi, P.S.; Vennestrom, P.N.R.; Falsig, H.; Jensen, A.D.; Janssens, T.V.W. Importance of the Cu oxidation state for the SO₂-poisoning of a Cu-SAPO-34 catalyst in the NH₃-SCR reaction. *Appl. Catal. B Environ.* **2018**, *236*, 377–383. [[CrossRef](#)]
6. Jangjou, Y.; Do, Q.; Gu, Y.; Lim, L.-G.; Sun, H.; Wang, D.; Kumar, A.; Li, J.; Grabow, L.C.; Epling, W.S. Nature of Cu Active Centers in Cu-SSZ-13 and Their Responses to SO₂ Exposure. *ACS Catal.* **2018**, *8*, 1325–1337. [[CrossRef](#)]
7. Wang, L.; Huang, B.; Su, Y.; Zhou, G.; Wang, K.; Luo, H.; Ye, D. Manganese oxides supported on multi-walled carbon nanotubes for selective catalytic reduction of NO with NH₃: Catalytic activity and characterization. *Chem. Eng. J.* **2012**, *192*, 232–241. [[CrossRef](#)]
8. Liu, C.; Shi, J.-W.; Gao, C.; Niu, C. Manganese oxide-based catalysts for low-temperature selective catalytic reduction of NO_x with NH₃: A review. *Appl. Catal. A Gen.* **2016**, *522*, 54–69. [[CrossRef](#)]
9. Wang, C.; Sun, L.; Cao, Q.; Hu, B.; Huang, Z.; Tang, X. Surface structure sensitivity of manganese oxides for low-temperature selective catalytic reduction of NO with NH₃. *Appl. Catal. B Environ.* **2011**, *101*, 598–605. [[CrossRef](#)]
10. Jiang, B.; Liu, Y.; Wu, Z. Low-temperature selective catalytic reduction of NO on MnO_x/TiO₂ prepared by different methods. *J. Hazard. Mater.* **2009**, *162*, 1249–1254. [[CrossRef](#)]
11. Chang, H.; Chen, X.; Li, J.; Ma, L.; Wang, C.; Liu, C.; Schwank, J.W.; Hao, J. Improvement of Activity and SO₂ Tolerance of Sn-Modified MnO_x-CeO₂ Catalysts for NH₃-SCR at Low Temperatures. *Environ. Sci. Technol.* **2013**, *47*, 5294–5301. [[CrossRef](#)]
12. Marban, G.; Fuertes, A.B. Kinetics of the low-temperature selective catalytic reduction of NO with NH₃ over activated carbon fiber composite-supported iron oxides. *Catal. Lett.* **2002**, *84*, 13–19. [[CrossRef](#)]
13. Li, L.; Sun, B.; Sun, J.; Yu, S.; Ge, C.; Tang, C.; Dong, L. Novel MnO_x-CeO₂ nanosphere catalyst for low-temperature NH₃-SCR. *Catal. Commun.* **2017**, *100*, 98–102. [[CrossRef](#)]
14. Yu, C.; Hou, D.; Huang, B.; Lu, M.; Peng, R.; Zhong, Z. A MnO_x@Eu-CeO_x nanorod catalyst with multiple protective effects: Strong SO₂-tolerance for low temperature DeNO_x processes. *J. Hazard. Mater.* **2020**, *399*, 123011. [[CrossRef](#)] [[PubMed](#)]
15. Ji, B.; Lee, J.; Kwak, S.-Y. Manganese oxides with hierarchical structures derived from coordination polymers and their enhanced catalytic activity at low temperature for selective catalytic reduction of NO_x. *Dalton Trans.* **2019**, *48*, 16395–16401. [[CrossRef](#)] [[PubMed](#)]

16. Fickel, D.W.; D'Addio, E.; Lauterbach, J.A.; Lobo, R.F. The ammonia selective catalytic reduction activity of copper-exchanged small-pore zeolites. *Appl. Catal. B Environ.* **2011**, *102*, 441–448. [[CrossRef](#)]
17. Kwak, J.H.; Tonkyn, R.G.; Kim, D.H.; Szanyi, J.; Peden, C.H.F. Excellent activity and selectivity of Cu-SSZ-13 in the selective catalytic reduction of NO_x with NH₃. *J. Catal.* **2010**, *275*, 187–190. [[CrossRef](#)]
18. Korhonen, S.T.; Fickel, D.W.; Lobo, R.F.; Weckhuysen, B.M.; Beale, A.M. Isolated Cu²⁺ ions: Active sites for selective catalytic reduction of NO. *Chem. Commun.* **2011**, *47*, 800–802. [[CrossRef](#)] [[PubMed](#)]
19. Buchholz, A.; Wang, W.; Xu, M.; Arnold, A.; Hunger, M. Thermal stability and dehydroxylation of Bronsted acid sites in silicoaluminophosphates H-SAPO-11, H-SAPO-81 H-SAPO-31, and H-SAPO-34 investigated by multi-nuclear solid-state NMR spectroscopy. *Microporous Mesoporous Mater.* **2002**, *56*, 267–278. [[CrossRef](#)]
20. Li, R.; Wang, P.; Ma, S.; Yuan, F.; Li, Z.; Zhu, Y. Excellent selective catalytic reduction of NO_x by NH₃ over Cu/SAPO-34 with hierarchical pore structure. *Chem. Eng. J.* **2020**, *379*, 122376. [[CrossRef](#)]
21. Liu, J.; Yu, F.; Liu, J.; Cui, L.; Zhao, Z.; Wei, Y.; Sun, Q. Synthesis and kinetics investigation of meso-microporous Cu-SAPO-34 catalysts for the selective catalytic reduction of NO with ammonia. *J. Environ. Sci.* **2016**, *48*, 45–58. [[CrossRef](#)] [[PubMed](#)]
22. Guo, K.; Fan, G.; Gu, D.; Yu, S.; Ma, K.; Liu, A.; Tan, W.; Wang, J.; Du, X.; Zou, W.; et al. Pore Size Expansion Accelerates Ammonium Bisulfate Decomposition for Improved Sulfur Resistance in Low-Temperature NH₃-SCR. *ACS Appl. Mater. Interfaces* **2019**, *11*, 4900–4907. [[CrossRef](#)]
23. Arstad, B.; Lind, A.; Cavka, J.H.; Thorshaug, K.; Akporiaye, D.; Wragg, D.; Fjellvag, H.; Gronvold, A.; Fuglerud, T. Structural changes in SAPO-34 due to hydrothermal treatment. A NMR, XRD, and DRIFTS study. *Microporous Mesoporous Mater.* **2016**, *225*, 421–431. [[CrossRef](#)]
24. Jin, H.X.; Gu, X.J.; Hong, B.; Lin, L.S.; Wang, C.Y.; Jin, D.F.; Peng, X.L.; Wang, X.Q.; Ge, H.L. Fabrication of Mesoporous Co₃O₄ from LP-FDU-12 via Nanocasting Route and Effect of Wall/Pore Size on Their Magnetic Properties. *J. Phys. Chem. C* **2012**, *116*, 13374–13381. [[CrossRef](#)]
25. Shao, J.; Cheng, S.; Li, Z.; Huang, B. Enhanced Catalytic Performance of Hierarchical MnO_x/ZSM-5 Catalyst for the Low-Temperature NH₃-SCR. *Catalysts* **2020**, *10*, 311. [[CrossRef](#)]
26. Tian, J.; Peng, H.; Xu, X.; Liu, W.; Ma, Y.; Wang, X.; Yang, X. High surface area La₂Sn₂O₇ pyrochlore as a novel, active and stable support for Pd for CO oxidation. *Catal. Sci. Technol.* **2015**, *5*, 2270–2281. [[CrossRef](#)]
27. Zhang, Z.P.; Li, R.M.; Wang, M.J.; Li, Y.S.; Tong, Y.M.; Yang, P.P.; Zhu, Y.J. Two steps synthesis of CeTiO_x oxides nanotube catalyst: Enhanced activity, resistance of SO₂ and H₂O for low temperature NH₃-SCR of NO_x. *Appl. Catal. B Environ.* **2021**, *282*, 119542. [[CrossRef](#)]
28. Gao, J.; Han, Y.; Mu, J.; Wu, S.; Tan, F.; Shi, Y.; Li, X. 2D, 3D mesostructured silicas templated mesoporous manganese dioxide for selective catalytic reduction of NO_x with NH₃. *J. Colloid Interface Sci.* **2018**, *516*, 254–262. [[CrossRef](#)]
29. Yu, J.; Guo, F.; Wang, Y.; Zhu, J.; Liu, Y.; Su, F.; Gao, S.; Xu, G. Sulfur poisoning resistant mesoporous Mn-base catalyst for low-temperature SCR of NO with NH₃. *Appl. Catal. B Environ.* **2010**, *95*, 160–168. [[CrossRef](#)]
30. Zhang, D.; Zhang, L.; Shi, L.; Fang, C.; Li, H.; Gao, R.; Huang, L.; Zhang, J. In situ supported MnO_x-CeO_x on carbon nanotubes for the low-temperature selective catalytic reduction of NO with NH₃. *Nanoscale* **2013**, *5*, 1127–1136. [[CrossRef](#)]
31. Jin, W.; Wang, B.; Tuo, P.; Li, C.; Li, L.; Zhao, H.; Gao, X.; Shen, B. Selective Desilication, Mesopores Formation, and MTO Reaction Enhancement via Citric Acid Treatment of Zeolite SAPO-34. *Ind. Eng. Chem. Res.* **2018**, *57*, 4231–4236. [[CrossRef](#)]
32. Li, J.; Guo, J.; Shi, X.; Wen, X.; Chu, Y.; Yuan, S. Effect of aluminum on the catalytic performance and reaction mechanism of Mn/MCM-41 for NH₃-SCR reaction. *Appl. Surf. Sci.* **2020**, *534*, 147592. [[CrossRef](#)]
33. Qiu, M.; Zhan, S.; Yu, H.; Zhu, D.; Wang, S. Facile preparation of ordered mesoporous MnCo₂O₄ for low-temperature selective catalytic reduction of NO with NH₃. *Nanoscale* **2015**, *7*, 2568–2577. [[CrossRef](#)]
34. Sun, X.; Guo, R.-T.; Liu, J.; Fu, Z.-G.; Liu, S.-W.; Pan, W.-G.; Shi, X.; Qin, H.; Wang, Z.-Y.; Liu, X.-Y. The enhanced SCR performance of Mn/TiO₂ catalyst by Mo modification: Identification of the promotion mechanism. *Int. J. Hydrog. Energy* **2018**, *43*, 16038–16048. [[CrossRef](#)]
35. Chen, J.; Shen, M.; Wang, X.; Qi, G.; Wang, J.; Li, W. The influence of nonstoichiometry on LaMnO₃ perovskite for catalytic NO oxidation. *Appl. Catal. B Environ.* **2013**, *134*, 251–257. [[CrossRef](#)]
36. Yang, S.; Wang, C.; Li, J.; Yan, N.; Ma, L.; Chang, H. Low temperature selective catalytic reduction of NO with NH₃ over Mn-Fe spinel: Performance, mechanism and kinetic study. *Appl. Catal. B Environ.* **2011**, *110*, 71–80. [[CrossRef](#)]
37. Zhang, Q.; Xu, L.; Ning, P.; Gu, J.; Guan, Q. Surface characterization studies of CuO-CeO₂-ZrO₂ catalysts for selective catalytic reduction of NO with NH₃. *Appl. Surf. Sci.* **2014**, *317*, 955–961. [[CrossRef](#)]
38. Ren, Q.; Mo, S.; Peng, R.; Feng, Z.; Zhang, M.; Chen, L.; Fu, M.; Wu, J.; Ye, D. Controllable synthesis of 3D hierarchical Co₃O₄ nanocatalysts with various morphologies for the catalytic oxidation of toluene. *J. Mater. Chem. A* **2018**, *6*, 498–509. [[CrossRef](#)]
39. Jiang, B.Q.; Wu, Z.B.; Liu, Y.; Lee, S.C.; Ho, W.K. DRIFT Study of the SO₂ Effect on Low-Temperature SCR Reaction over Fe-Mn/TiO₂. *J. Phys. Chem. C* **2010**, *114*, 4961–4965. [[CrossRef](#)]
40. Wu, S.; Yao, X.; Zhang, L.; Cao, Y.; Zou, W.; Li, L.; Ma, K.; Tang, C.; Gao, F.; Dong, L. Improved low temperature NH₃-SCR performance of FeMnTiO_x mixed oxide with CTAB-assisted synthesis. *Chem. Commun.* **2015**, *51*, 3470–3473. [[CrossRef](#)]
41. Yang, S.; Guo, Y.; Yan, N.; Wu, D.; He, H.; Qu, Z.; Yang, C.; Zhou, Q.; Jia, J. Nanosized Cation-Deficient Fe-Ti Spinel: A Novel Magnetic Sorbent for Elemental Mercury Capture from Flue Gas. *ACS Appl. Mater. Interfaces* **2011**, *3*, 209–217. [[CrossRef](#)]

42. Liu, H.; Fan, Z.X.; Sun, C.Z.; Yu, S.H.; Feng, S.; Chen, W.; Chen, D.Z.; Tang, C.J.; Gao, F.; Dong, L. Improved activity and significant SO₂ tolerance of samarium modified CeO₂-TiO₂ catalyst for NO selective catalytic reduction with NH₃. *Appl. Catal. B Environ.* **2019**, *244*, 671–683. [[CrossRef](#)]
43. Lian, Z.; Liu, F.; Shan, W.; He, H. Improvement of Nb Doping on SO₂ Resistance of VO_x/CeO₂ Catalyst for the Selective Catalytic Reduction of NO_x with NH₃. *J. Phys. Chem. C* **2017**, *121*, 7803–7809. [[CrossRef](#)]
44. Li, B.; Ren, Z.; Ma, Z.; Huang, X.; Liu, F.; Zhang, X.; Yang, H. Selective catalytic reduction of NO by NH₃ over CuO-CeO₂ in the presence of SO₂. *Catal. Sci. Technol.* **2016**, *6*, 1719–1725. [[CrossRef](#)]
45. Bai, B.; Arandiyani, H.; Li, J. Comparison of the performance for oxidation of formaldehyde on nano-Co₃O₄, 2D-Co₃O₄, and 3D-Co₃O₄ catalysts. *Appl. Catal. B Environ.* **2013**, *142*, 677–683. [[CrossRef](#)]
46. Wu, Z.; Jin, R.; Liu, Y.; Wang, H. Ceria modified MnO_x/TiO₂ as a superior catalyst for NO reduction with NH₃ at low-temperature. *Catal. Commun.* **2008**, *9*, 2217–2220. [[CrossRef](#)]
47. Shao, J.; Lin, F.; Huang, Y.; Wang, Z.; Li, Y.; Chen, G.; Cen, K. MnO_x fabrication with rational design of morphology for enhanced activity in NO oxidation and SO₂ resistance. *Appl. Surf. Sci.* **2020**, *503*, 144064. [[CrossRef](#)]
48. Li, C.; Tang, X.; Yi, H.; Wang, L.; Cui, X.; Chu, C.; Li, J.; Zhang, R.; Yu, Q. Rational design of template-free MnO_x-CeO₂ hollow nanotube as de-NO_x catalyst at low temperature. *Appl. Surf. Sci.* **2018**, *428*, 924–932. [[CrossRef](#)]
49. Ma, Z.; Sheng, L.; Wang, X.; Yuan, W.; Chen, S.; Xue, W.; Han, G.; Zhang, Z.; Yang, H.; Lu, Y.; et al. Oxide Catalysts with Ultrastrong Resistance to SO₂ Deactivation for Removing Nitric Oxide at Low Temperature. *Adv. Mater.* **2019**, *31*, 1903719. [[CrossRef](#)]
50. Pan, S.; Luo, H.; Li, L.; Wei, Z.; Huang, B. H₂O and SO₂ deactivation mechanism of MnO_x/MWCNTs for low-temperature SCR of NO_x with NH₃. *J. Mol. Catal. A Chem.* **2013**, *377*, 154–161. [[CrossRef](#)]